

Keto-anthraquinone covalent organic framework for H₂O₂ photosynthesis with oxygen and alkaline water

Lizhi Zhang

zhanglizhi@sjtu.edu.cn

Shanghai Jiao Tong University

Xiangcheng Zhang

Shanghai Jiao Tong University

Silian Cheng

Shanghai Jiao Tong University

Chao chen

Shanghai Engineering Research Center of Biotransformation of Organic Solid Waste, Shanghai Key Lab for Urban Ecological Processes and Eco-Restoration, School of Ecological and Environmental Science

Xue Wen

Shanghai Jiao Tong University

Jie Miao

Shanghai Jiao Tong University

Baoxue zhou

School of Environmental Science and Engineering, Key Laboratory of Thin Film and Microfabrication Technology (Ministry of Education), Shanghai Jiao Tong University <https://orcid.org/0000-0001-9691-3119>

Mingce Long

Shanghai Jiao Tong University <https://orcid.org/0000-0002-5168-8330>

Article

Keywords:

Posted Date: December 2nd, 2023

DOI: <https://doi.org/10.21203/rs.3.rs-3678746/v1>

License:   This work is licensed under a Creative Commons Attribution 4.0 International License.

[Read Full License](#)

Additional Declarations: There is **NO** Competing Interest.

Version of Record: A version of this preprint was published at Nature Communications on March 26th, 2024. See the published version at <https://doi.org/10.1038/s41467-024-47023-y>.

Abstract

Hydrogen peroxide (H_2O_2) photosynthesis is an attractive carbon-neutral process for decentralized applications, but suffers from insufficient activity of catalysts due to the high energy barrier of hydrogen extraction from H_2O without sacrificial reagent. Herein, we report that mechanochemically synthesized keto-form anthraquinone covalent organic framework (Kf-AQ) is able to directly synthesize H_2O_2 with molecular oxygen and alkaline water ($\text{pH} = 13$) in the absence of any sacrificial reagents, with a superior production rate of $4784 \mu\text{mol h}^{-1} \text{g}^{-1}$ under visible light irradiation ($\lambda > 400 \text{ nm}$) and an impressive apparent quantum yield (AQY) of 15.8% at 400 nm. Characterization results revealed that the strong alkalinity resulted in the formation of $\text{OH}^-(\text{H}_2\text{O})_n$ clusters in water, which were first adsorbed on keto moieties of Kf-AQ and then more easily dissociated into molecular oxygen and active hydrogen with the injection of photoelectrons, because the energy barrier of hydrogen extraction from $\text{OH}^-(\text{H}_2\text{O})_n$ was largely lowered by weakening the H-bonded networks of H_2O molecules owing to the excessive electrons in OH^- . The produced active hydrogen quickly diffused to react with anthraquinone to generate anthrahydroquinone, which was subsequently oxidized by molecular oxygen to selectively produce H_2O_2 . This study provides a novel efficient H_2O_2 photosynthesis material, and also sheds light on the importance of hydrogen extraction from H_2O for photocatalytic H_2O_2 synthesis.

Introduction

Hydrogen peroxide (H_2O_2), a chemical with increasing market share, finds extensive applications in biomedicine, disinfection, bleaching, organic synthesis, and water treatment¹⁻⁴. The well-known industrial production of H_2O_2 is the anthraquinone (AQ) process, which suffers from intensive energy consumption and waste discharge⁵. As a green and carbon-neutral alternative, solar driven oxygen reduction strategy of H_2O_2 synthesis from molecular oxygen and water attracts more and more attention⁶⁻⁹. Although many photocatalysts are effective for the H_2O_2 synthesis, high dosages of organic sacrificial reagents such as isopropanol are always used to scavenge photogenerated holes and offer hydrogen for the H_2O_2 formation, which obviously bring in undesired impurity and also increase the cost of H_2O_2 synthesis¹⁰. In comparison with organic sacrificial reagents, water is more inexpensive and convenient hydrogen source, but an intrinsically poor hydrogen donor, because water molecules have a high O-H bond dissociation energy (BDE, 492 kJ mol^{-1} for homolytic cleavage)^{11,12}. Thus, highly efficient H_2O_2 photosynthesis only with molecular oxygen and water is of great significance, but remains a giant challenge.

It is well known that the hydrogen-bond (H-bond) in adsorbed water clusters plays critical role on water dissociation during photocatalysis^{13,14}. At a "pseudodissociated" state¹⁴, the intermolecular H-bond facilitates the cleavage of water O-H bond at < 1 monolayer coverage¹⁵, and interface H-bond also promotes photogenerated hole transfer and water oxidation by the strongly coupling of H-bond with holes¹⁶. Unfortunately, strong hydrogen bond network among water clusters inhibits the water

dissociation¹⁷. Thus, an accurate control of H-bond network and adsorbed water monolayers over photocatalysts is vital for water dissociation¹³. Recently, scientists found that excess electrons of OH⁻ anions in alkaline water could induce reorganization of hydrogen bond in water clusters, thus further diminishing the overall energy barrier of alkaline hydrogen evolution reaction (HER)¹⁸. However, it is still unknown whether this alkaline based H-bond network manipulation strategy is feasible for the H₂O₂ photosynthesis.

Different from traditional metal oxide photocatalysts of poor interfacial H-bond modulation capacity, covalent organic frameworks (COFs), famous metal-free molecular photocatalysts possessing huge potential in H₂O₂ photosynthesis, are very powerful to regulate H-bond at molecular levels because of their variable and designable organic units^{19,20}. Among various organic units, AQ moieties is believed to be the best redox center for the H₂O₂ synthesis, as the oxidation of the hydrogenated AQ (anthrahydroquinone, HAQ) by molecular oxygen can selectively produce H₂O₂, which is thermodynamically spontaneous and commercially used⁵. Recently, several AQ-containing COFs (such as TPE-AQ, TpAQ, AQTEE-COP, and AQTT-COP) were designed to promote photogenerated charge separation and facilitate WOR for efficient H₂O₂ photosynthesis with pure water upon visible light irradiation (> 400 nm), and their best activity reached 3221 $\mu\text{mol g}^{-1} \text{h}^{-1}$ without manipulating H-bond network²¹⁻²⁴.

As a typical AQ-containing COFs, TpAQ synthesized by β -ketoenamines links of 2,6-diaminoanthraquinone (AQ) and 2, 4, 6-triformylphloroglucinol (Tp), is often a mixture of keto- and enol-forms due to the formation of tautomerism during the polymerization (Fig. S1). Different from the unstable enol-form that mainly form weak H-bond with oxygen in H₂O²⁵, keto-form AQ COFs (Kf-AQ) is a more favorable proton acceptor to combine with hydrogen in H₂O via strong H-bond. Generally, traditional solvothermal method with acetic acid catalysis tends to produce enol-form dominant COFs. Although alkaline solution (such as OH⁻) induces the transformation of enol-form into keto-form²⁶, the NaOH addition disfavored the solvothermal synthesis of Kf-AQ, because the excessive solvents would consume NaOH to form carboxylates. Thus, the controlled synthesis of Kf-AQ is crucial for superior H₂O₂ photosynthesis, but never reported previously.

Herein we demonstrate the first mechanochemical synthesis of keto-form anthraquinone covalent organic framework (Kf-AQ) for direct H₂O₂ photosynthesis with molecular oxygen and alkaline water (pH = 13), and this Kf-AQ could deliver a record H₂O₂ production rate of 4784 $\mu\text{mol h}^{-1} \text{g}^{-1}$ in the absence of any sacrificial reagents under visible light irradiation ($\lambda > 400 \text{ nm}$). The critical roles of hydroxide anions and keto-form AQ moieties for efficient H₂O₂ production are carefully clarified via in-situ characterization and theory calculations.

Results

Synthesis and structure characterization. Kf-AQ was mechanochemically synthesized by a Schiff-base condensation reaction of Tp and AQ with CH₃COONa (NaAc) as the catalysts (Fig. 1a). Fourier-transformed infrared spectra (FT-IR) spectra clearly revealed a new C-N stretching band at 1260 cm⁻¹ and a disappeared N-H stretching band at 3459 ~ 3151 cm⁻¹ for NH₂ groups in AQ (Fig. S2)²⁷. The as-prepared Kf-AQ powder displays a red-black color, corresponding to its outstanding optical absorption with the edge extended to 900 nm (Fig. S3), which is obviously red-shifted as compared to the absorption edge at 780 nm of TpAQ prepared by a traditional solvothermal method²⁸. The simulated powder X-ray diffraction (PXRD) pattern of Kf-AQ with eclipsed AA stacking mode agreed well with the experimental data (Fig. 1b), suggesting the validity of such structure in Kf-AQ. Particularly, the broad peak at 26.54° was caused by the strong π - π stacking construction arisen from the existence of a multilayered COF structure with an interlayer distance of 3.48 Å. TEM and SEM images also displayed that Kf-AQ had a lamellar stacking structure and excellent crystallinity (Fig. 1c, d and Fig. S4)²⁸. Moreover, Kf-AQ had a specific surface area of 129 m² g⁻¹ and a pore size of 2.12 nm (Fig. S5), which was well matched with the simulated value (2.18 nm) in Fig. 1a.

Solid-state NMR spectra revealed that Kf-AQ had an almost exclusive keto-form structure (Fig. 1e). The chemical shifts at 184 ppm, 144 ppm and 109 ppm in ¹³C NMR spectra were all indexed to the keto-form structure of Kf-AQ^{25,27,29}, while the chemical shift at 4.4 ppm for the enol-form (c, C-OH) was absent in the ¹H NMR spectra (Fig. S6)³⁰. Only C, O and N elements were present in the XPS survey spectrum of Kf-AQ, without any residual Na (Fig. S7). More evidences of keto-form structure in Kf-AQ could be found in high resolution XPS spectra (Fig. S8). The content of C = O in Kf-AQ was approximately 60%, about three times that of C-OH (22%) (Fig. 1f). The content of C-N-H (56%), corresponding to the deconvolution peak at the binding energy of 400.4 eV in N 1s spectra, was obviously higher than that of C = N (31%) (Fig. S9a)³¹, while C 1s XPS spectra also illustrated more C-C (52%) and less C-O (38%) in Kf-AQ (Fig. S9b)³². All these above results supported the successful synthesis of an exclusive keto-form AQ COF.

The formation of Kf-AQ might be attributed to a NaAc-catalyzed Schiff-base condensation process as follows. Upon the heat generated from the collision of balls, the carbonyl oxygen on Tp monomer undergoes a nucleophilic addition with Na⁺ to form aldehyde salts^{33,34}, resulting in the neighbor carbon acquiring a positive charge to fulfill another nucleophilic addition with nitrogen atoms in AQ. The generated α -hydroxyl undergoes further dehydration with adjacent amino hydrogen to form an enol-form COF. Subsequently, Ac⁻ anions as the Lewis base tend to bind with the hydrogen of hydroxyl group in enol moieties and then induce electron transfer from oxygen to alkene group, thus enabling the enol-form transformation into the thermodynamically more stable keto-form moiety (Fig. S10). Such a transformation cannot be driven in the traditional solvothermal synthesis, but might partially occur in alkaline water to produce a keto-form dominated AQ COF^{25,35}.

Efficient H₂O₂ photosynthesis. The H₂O₂ photosynthesis performance of Kf-AQ was evaluated by dispersing the powder in water at neutral and alkaline solutions (pH = 9, 11, 13, 14) with continuous O₂

purging. Upon visible light ($\lambda > 400$ nm) irradiation, the rate of H_2O_2 production at pH 13 reached as high as $4784 \mu\text{mol h}^{-1} \text{g}^{-1}$ (Fig. 2a), a new record in H_2O_2 photosynthesis of AQ containing COFs with water (Fig. 2b and Table S1). Upon a prolonged irradiation for 5 h, the H_2O_2 production was steadily growing (Fig. S11), and kept constant during five cycles of reaction (Fig. 2c). The crystal structure and surface functional groups of the reacted Kf-AQ did not change (Fig. S12), demonstrating its excellent stability for the H_2O_2 photosynthesis. The contribution of Na^+ to the enhanced H_2O_2 production was ruled out by the replacement of NaOH with NaCl and KOH (Fig. S13), confirming the crucial promoting effect of hydroxide anions on the H_2O_2 photosynthesis of Kf-AQ.

The kinetic of H_2O_2 production was analyzed by fitting the time-dependent H_2O_2 production curves (Text S2). Kf-AQ exhibited the highest H_2O_2 formation rate constant (k_f , $31.39 \mu\text{M min}^{-1}$), but a medium decomposition rate constant (k_d) ($0.031 \mu\text{M min}^{-1}$) at pH 13 (Fig. 2d and Table S2). Thus, the superior H_2O_2 photosynthesis performance of Kf-AQ with alkaline water was mainly attributed to its better H_2O_2 formation ability. The apparent quantum efficiencies (AQY) of Kf-AQ at different wavelengths were well matched with its absorption spectrum, and the highest value appeared at 400 nm and reached 15.8% (Fig. 2e and Table S3). To the best of our knowledge, the AQY of Kf-AQ is higher than those of most reported H_2O_2 synthesis photocatalysts^{36,37}. The solar-to-chemical conversion (SCC) efficiency of Kf-AQ was estimated to be 0.70% at pH 13 (Fig. S14 and Table S4), which was almost seven times of the average solar-to-biomass conversion (SBC) efficiency in nature²³.

Mechanism investigation. We first checked the basic semiconductor properties of Kf-AQ to understand its superior performance in H_2O_2 photosynthesis. The Tauc plot showed that the band gap of Kf-AQ was 1.55 eV (Fig. S15a), and ultraviolet photoelectron spectroscopy (UPS) determined its valence band potential (E_{VB}) as 1.90 V (Fig. S15b), suggesting that the conduction band potential (E_{CB}) of Kf-AQ was accordingly calculated as 0.35 V. Therefore, both 2e^- ORR (0.68 V vs. RHE) to produce H_2O_2 and 4e^- WOR (1.23 V vs. RHE) to evolve O_2 were thermodynamically feasible for Kf-AQ photocatalysis (Fig. 3a)³⁸. We further conducted density functional theory (DFT) calculations to elucidate the exciton dissociation in photocatalysis by using a dimer model of Kf-AQ. As depicted in Fig. 3b, the highest occupied molecular orbital (HOMO) of the dimer uniformly dispersed in the whole structure, while the lowest unoccupied molecular orbital (LUMO) localized over AQ units. Thus, the HOMO-LUMO transition under excitation can redistribute electron density from the Tp moieties to the adjacent AQ units, thus resulting in effective intramolecular charge transfer in Kf-AQ.

We then explored the sources of H and O for the H_2O_2 production by various control experiments and isotopic labeling analysis. In comparison to oxygen atmosphere, either air or N_2 purging resulted in poor H_2O_2 production (Fig. 3c), and the O_2 concentration in an airtight oxygen saturated suspension decreased obviously during photocatalysis (Fig. S16), suggesting the dominated contribution of ORR to the H_2O_2 production. AgNO_3 was added as the electron scavenger in N_2 atmosphere to evaluate the contribution of water oxidation. The negligible amount of H_2O_2 generated in the Kf-AQ suspension ruled out the direct

contribution of WOR to the H_2O_2 production. However, H_2O_2 was obviously produced in case of N_2 purging and absence of AgNO_3 , suggesting that photocatalytically produced O_2 via 4e^- WOR (Fig. 3c) enabled the consequent ORR to produce H_2O_2 (Fig. S17). Significant H_2O_2 was only detected in the mixed solution of H_2O and acetonitrile ($v/v = 1:1$) other than pure acetonitrile (Fig. 3d), confirming that water was the exclusive hydrogen source for the H_2O_2 photosynthesis.

We conducted the isotopic photoreaction experiments by purging H_2^{16}O suspensions with $^{18}\text{O}_2$ gas during the H_2O_2 photosynthesis, and then used MnO_2 to catalytically decompose the as-synthesized H_2O_2 into oxygen. After 8 h of photoreaction, strong $^{18}\text{O}_2$ ($m/z = 36$, 93.7%) and very weak $^{16}\text{O}_2$ ($m/z = 32$, 6.3%) signals appeared in the gas chromatography-mass spectra (GC-MS) of collected gas (Fig. 3e), demonstrating that $\text{H}_2^{18}\text{O}_2$ was the dominated product and mainly came from the reduction of $^{18}\text{O}_2$. Gradually, the signal of $^{18}\text{O}_2$ peak decreased (80.5%), accompanying with an increased $^{16}\text{O}_2$ signal (19.5%) at 24 h of reaction, because the photocatalytic oxidation of H_2^{16}O produced $^{16}\text{O}_2$ to increase the proportion of $\text{H}_2^{16}\text{O}_2$ in the products. The electrons transfer number (n) of ORR was further measured to be about 2.06 ~ 2.09 by the RDE method (Fig. 3f and Fig. S18)²⁴. Thus, we suppose that both 2e^- ORR and 4e^- WOR take place during H_2O_2 photosynthesis over Kf-AQ at pH 13.

To probe the active sites of Kf-AQ for the H_2O_2 photosynthesis, we synthesized two control COFs by respectively replacing the monomers of Tp and AQ with 1,3,5-trimethylbenzaldehyde (LZU) and 2,6-diaminoanthracene (DA), namely LZUAQ and TpDA (Fig. S19 and S20). Their H_2O_2 photosynthesis performance was much worse than that of Kf-AQ (Fig. S21), suggesting that anthraquinone groups were the indispensable active sites for ORR, and the keto and AQ conjugated configuration accounted for the efficient WOR over Kf-AQ.

We then employed in-situ FTIR and Raman spectra to further understand the critical role of water adsorption and dehydrogenation in the superior H_2O_2 photosynthesis of Kf-AQ. Upon irradiation, three obvious O-H stretching vibration bands appeared in the in-situ FTIR spectra of Kf-AQ (Fig. 4a), corresponding to the water clusters including $\text{Na}^+(\text{H}_2\text{O})_3$ or $\text{OH}^-(\text{H}_2\text{O})_3$ (3540 cm^{-1}), $\text{OH}^-(\text{H}_2\text{O})_4$ (3410 cm^{-1}), and $\text{OH}^-(\text{H}_2\text{O})_5$ (3292 cm^{-1})^{39,40}. These adsorbed water clusters were the proton precursors for H_2O_2 photosynthesis, which can be further checked by in-situ Raman spectra. The notable O-H stretching bands in Raman spectra at around $3000\text{--}3700\text{ cm}^{-1}$ can be deconvoluted into three bands, corresponding to the four-coordinated hydrogen bonded water network (V_1 , 3254 cm^{-1}), the two-coordinated single donor hydrogen bonded water clusters (V_2 , 3420 cm^{-1}) and the Na^+ ion hydrated water ($\text{Na}\cdot\text{H}_2\text{O}$) clusters (V_3 , 3553 cm^{-1}), respectively (Fig. 4b)⁴¹⁻⁴³. The intensity of these bands for Kf-AQ was significantly higher than those for TpAQ, suggesting the formation of stronger hydrogen bond between keto moiety ($-\text{C}=\text{O}$) and $\text{OH}^-(\text{H}_2\text{O})_n$ clusters⁴³, possibly because the vibrational dipole moment (the direction of O-H bonds) in the clusters (such as $\text{Na}\cdot\text{H}_2\text{O}$) is parallel to the direction of the interfacial electric field, thus favoring the combination of hydrogen in the clusters with carbonyl groups of Kf-AQ.

Simultaneously, V2 and V3 were the dominant forms in the Kf-AQ Raman spectrum, and generally had relatively weaker hydrogen bond network than V1, the dominant form in the TpAQ Raman spectrum. These differences can be attributed to the strong interaction between water clusters and carbonyl groups of Kf-AQ, resulting in the disorder and stretching of H-bonds in the arrangement of water molecules⁴⁴, and the strong dipole-dipole force between Na⁺ and H₂O molecules in the Na⁺ solvation structures further destroy the water-water interactions to form small water clusters of weak H-bonding environment⁴⁴, thus favoring the photocatalytic dissociation of water and release of hydrogen. Therefore, the unique exclusive keto-form of Kf-AQ enhanced the adsorption and dissociation of water, thereby promoting hydrogen abstraction from water for the H₂O₂ photosynthesis.

We compared water adsorption over Kf-AQ and TpAQ by DFT calculations. In case of one water molecule adsorption, the adsorption energy of Kf-AQ was -0.26 eV, much lower than that of TpAQ (-0.18 eV) (Fig. S22). Increasing water cluster sizes to (H₂O)₃, the adsorption energy of Kf-AQ decreased to -0.35 eV, and further decreased to -0.44 eV for the OH⁻(H₂O)₂ clusters, which was the dominant form of adsorbed water in alkaline water (Fig. S23), suggesting the superior water adsorption capability of Kf-AQ. Moreover, the bond energy of terminal H-O in OH⁻(H₂O)₂ form was 4.3 eV, much lower than that of (H₂O)₃ (5.9 eV) (Fig. 4c), suggesting the easier hydrogen dissociation from the terminal water, and thus favoring the subsequently combination with the neighboring H₂O to form hydronium ion (H₃O⁺)¹⁸.

We detected the intermediates of H^{*}_{ads} and OH_{ads} species by the cyclic voltammogram (CV) (Fig. 4d). The H^{*}_{ads} species generated in the reduction stage by reducing hydronium ion (H₃O⁺) were oxidized, corresponding to an oxidative peak at about 0.25 V vs. RHE^{45,46}. The oxidative peaks in the CV curves were more distinct with the increase of hydroxide anion concentrations, suggesting the increase of H^{*}_{ads} dosages at strong alkaline conditions¹⁸. Simultaneously, the reduction peak at 0.77 V was attributed to the reversible adsorbed OH_{ads} species, which were produced via the loss of electrons in OH⁻ (ref. 47). The OH_{ads} species would be stabilized by forming hydroxyl-water-alkali metal cation cluster (OH_{ads}-Na⁺-(H₂O)_n), thus accordingly preventing its depletion by H₃O⁺. Therefore, we propose that the dissociation of H₂O into H^{*}_{ads} and OH_{ads} species takes place in the 2e⁻ ORR and 4e⁻ WOR pathways.

These above results strongly suggest a synergism of keto and anthraquinone moieties in Kf-AQ for superior H₂O₂ photosynthesis from water and oxygen, as depicted in Fig. 5. Initially, OH⁻(H₂O)_n clusters preferentially adsorb onto the keto-form moieties in Kf-AQ, thus weakening the H-O bond of the terminal H₂O via forming the H-OH(H₂O)_{n-1}OH⁻ clusters and facilitating the dehydrogenation in water molecules. The detached protons then combine with the neighboring H₂O to form H₃O⁺. Upon visible light irradiation, surface H₃O⁺ on Kf-AQ can be reduced by interfacial electrons (e⁻) to release H^{*}_{ads} species, which preferentially bind with the quinone groups (-C = O) in AQ and subsequently hydrogenate AQ to yield anthrahydroquinone (H₂AQ). Afterwards, the parahydrogen atoms of H₂AQ are abstracted to produce radicals, which react with O₂ to form 1,4-endoperoxide species, a well-known intermediate for the

formation of H_2O_2 , which was confirmed by the new Raman peak at 891 cm^{-1} (Fig. S24). Then, 1,4-endoperoxide species couples the adjacent hydrogen in the hydroxyl group of H_2AQ to release H_2O_2 . Meanwhile, another dissociation product, OH_{ads} intermediate, would not be dissociated as OH^- within the interface layer, but form an adsorbed hydroxyl-water-alkali metal cation cluster $(\text{OH}_{\text{ads}}\text{-Na}^+\text{-(H}_2\text{O)}_n)^{47}$. Upon visible light irradiation, the photogenerated holes (h^+) oxidizes this OH_{ads} to produce O_2 in a 4e^- WOR pathway. Therefore, the formation of $\text{OH}_{\text{ads}}\text{-Na}^+\text{-(H}_2\text{O)}_n$ and H_3O^+ intermediates over Kf-AQ at high pH conditions facilitates water oxidation and hydrogen extraction from H_2O molecules, resulting in its superior photocatalytic H_2O_2 production.

Discussion

We have demonstrated the synthesis of a keto-form anthraquinone containing COF via a mechanochemical process and its superior H_2O_2 photosynthesis in alkaline water, with a record H_2O_2 production rate of $4784\text{ }\mu\text{mol h}^{-1}\text{ g}^{-1}$ under visible light irradiation in the absence of sacrificial reagents. The keto-form structure in Kf-AQ can promote the water adsorption through the formation of $\text{OH}^-\text{(H}_2\text{O)}_n$ clusters with weakened hydrogen bonds, which accordingly enhances the dehydrogenation of water and promotes efficient H_2O_2 photosynthesis. The manipulating H-bond network of adsorbed water clusters represents a novel strategy to break the rate-limiting step of hydrogen extraction from water, and bring insights for the design of highly active photocatalysts to realize efficient H_2O_2 photosynthesis from only water and oxygen.

Methods

Synthesis of Kf-AQ. Mechanochemical synthesis was conducted to produce Kf-AQ by use of a planetary ball mill (SFM-1, Hefei Kejing Material Technology Co., Ltd). Typically, 2,4,6-triformylphloroglucinol (Tp, 126 mg, 0.20 mmol), 2,6-diaminoanthraquinone (AQ, 213 mg, 0.30 mmol), and CH_3COONa (5 mg) were placed in a 50 mL agate grinding jar, with fifteen 7 mm diameter and ten 5 mm diameter agate balls. Then, the mixture was ground at room temperature with a rotation speed of 400 rpm for 6 h. After that, the obtained precursors were washed with N, N-dimethylformamide and acetone, and then dried in a vacuum oven at $120\text{ }^\circ\text{C}$ for 12 h. The obtained photocatalyst was denoted as Kf-AQ.

Synthesis of TpAQ. TpAQ was synthesized by Schiff-base condensation of Tp and AQ according to a modified previous method²⁸. In a 10 mL Schlenk tube, 2,4,6-triformylphloroglucinol (71.4 mg, 0.20 mmol) and 2,6-diaminoanthraquinone (42.1 mg 0.30 mmol) were charged. Then, N, N-dimethylacetamide (2.0 mL) was added as the solvent, and the suspensions were sonicated for 10 min. Subsequently, 0.3 mL glacial acetic acid was added. After that, the ampoule was degassed by freeze-pump-thaw three times and then sealed on. The Schlenk tube was put into an oven and heated at $120\text{ }^\circ\text{C}$ for 72 h. The obtained powder was washed with N, N-dimethylformamide and acetone, and then dried in a vacuum oven at $120\text{ }^\circ\text{C}$ for 12 h.

H₂O₂ photosynthesis. H₂O₂ photosynthesis was conducted in a homemade quartz cuvette reactor. Generally, 5 mg of the photocatalysts were ultrasonically dispersed into 30 mL water whose initial pH was adjusted by 0.1 M NaOH solution. Then, the suspension was stirred for 15 min in the dark with continuously O₂ purging. After that, the reactor was illuminated by a 300 W Xe lamp (PLS-SXE300, Beijing Perfectlight) with a cut-off filter ($\lambda > 400$ nm). During the reaction, 1.5 mL of reaction mixture was withdrawn at every 15 min interval, and then filtrated through a 0.45 μ m polyether sulfone (PES) filter for H₂O₂ detection.

The H₂O₂ concentration was measured by the N, N-diethylp-phenylenediamine (DPD)-horseradish peroxidase (POD) colorimetry method⁴⁸. Typically, 3.0 mL of phosphate buffer (0.2 M, pH = 6) was added into a 15.0 mL colorimetric tube, and then 1.0 mL sample, 50 μ L DPD, 50 μ L POD were all added into the mixture. Then, ultrapure water was added to set the volume to 10 mL. Finally, the absorbance was measured on a UV-vis spectrophotometer (TU-1810) at 551 nm to determine H₂O₂ concentration according to the predetermined standard curve.

In-situ FTIR measurements. In-situ FTIR spectra were obtained by using a Thermo Scientific Nicolet Is50, equipped with a commercial chamber from Harrick Scientific. Typically, 5 mg of Kf-AQ was dispersed into 30 mL H₂O at pH = 13. The formed uniform dispersion was bubbled with O₂ for 15 min in the dark, and then the background spectrum was collected. After that, the reaction chamber was irradiated by visible light ($\lambda > 400$ nm), and then the spectrum was collected at a one min interval.

Isotopic experiments. Specifically, 5 mg Kf-AQ was added into H₂¹⁶O (30 mL) within a glass tube (50 mL). The formed dispersion was sonicated for 10 min and bubbled with Ar for 30 min. Then, the reaction tube was sealed with rubber septum cap and vacuum. ¹⁸O₂ gas was introduced to the tube by a syringe. The reaction tube was illuminated by a 300 W Xe lamp with a cut-off filter ($\lambda > 400$ nm). After photoreaction for 8 h and 24 h, the reaction solution was purged by Ar for 5 min to remove the residual ¹⁸O₂ gas. The dispersion was filtered and injected into another clean tube, which was saturated with Ar and contained 200 mg MnO₂ powder. The generated gas was collected by an Aluminum foil air pocket (5 mL) and detected on a Shimadzu GC-MS system (Agilent 7890 A/ 5975C).

DFT calculations. The DFT calculation used the method in previous references⁴⁹. Briefly, geometry optimizations without symmetry restriction are performed by using the DFT/B3LYP/6-31G(d, p) basis sets and scrf-smd solvent model. All calculations were performed on Gaussian 09.

Declarations

Data availability

Source data are provided with this paper. The data that support the findings of this study are available from the corresponding author upon reasonable request.

Competing interests

The authors declare no competing interests.

Additional Information

Supplementary Information is available online or from the author.

Author contributions

X. Z., M. L., B. Z., and L. Z. contributed to design of this study, X. Z., M. L., and L. Z. wrote the manuscript. X. Z., J. M., C. C., and S. C. conducted experiments and performed data analysis. X. W. provided DFT calculations and analysis.

Acknowledgement

Financial supports from the National Natural Science Foundation of China (Nos. 22376138, 22206125, 52070128) and National Key R&D Program of China (2022YFA1205602) are gratefully acknowledged.

References

1. Sun X et al (2022) Molecular oxygen enhances H₂O₂ utilization for the photocatalytic conversion of methane to liquid-phase oxygenates. *Nat Commun* 13:6677
2. Shi X et al (2021) Electrochemical synthesis of H₂O₂ by two-electron water oxidation reaction. *Chem* 7:38–63
3. Wang X, Du J, Xu C (2021) Reactions in activated peroxide systems and their influences on bleaching performance. *Mini-Rev Org Chem* 18:836–840
4. Xu J et al (2020) Organic wastewater treatment by a single-atom catalyst and electrolytically produced H₂O₂. *Nat Sustain* 4:233–241
5. Campos-Martin JM, Blanco-Brieva G, Fierro JL (2006) Hydrogen peroxide synthesis: an outlook beyond the anthraquinone process. *Angew Chem Int Ed* 45:6962–6984
6. Chen Z, Yao D, Chu C, Mao S (2023) Photocatalytic H₂O₂ production systems: design strategies and environmental applications. *Chem Eng J* 451:138489
7. Kondo Y, Kuwahara Y, Mori K, Yamashita H (2022) Design of metal-organic framework catalysts for photocatalytic hydrogen peroxide production. *Chem* 8:2924–2938
8. Wu S, Quan X (2022) Design principles and strategies of photocatalytic H₂O₂ production from O₂ reduction. *ACS ES&T Eng* 2:1068–1079

9. Zeng X, Liu Y, Hu X, Zhang X (2021) Photoredox catalysis over semiconductors for light-driven hydrogen peroxide production. *Green Chem* 23:1466–1494
10. Zhao Y et al (2023) Efficient exciton dissociation in ionically interacted methyl viologen and polymeric carbon nitride for superior H₂O₂ photoproduction. *ACS Catal* 5:2790–2801
11. Agarwal RG et al (2022) Free energies of proton-coupled electron transfer reagents and their applications. *Chem Rev* 122:1–49
12. Zhang J, Muck-Lichtenfeld C, Studer A (2023) Photocatalytic phosphine-mediated water activation for radical hydrogenation. *Nature* 619:506–513
13. Ma X et al (2022) Hydrogen-bond network promotes water splitting on the TiO₂ surface. *J Am Chem Soc* 144:13565–13573
14. Du Y et al (2009) Two pathways for water interaction with oxygen adatoms on TiO₂(110). *Phys Rev Lett* 102:096102
15. Tan S et al (2020) Interfacial hydrogen-bonding dynamics in surface-facilitated dehydrogenation of water on TiO₂(110). *J Am Chem Soc* 142:826–834
16. Chu W et al (2022) Ultrafast charge transfer coupled to quantum proton motion at molecule/metal oxide interface. *Sci Adv* 8:eabo2675
17. Wang Y et al (2022) Enabling high-energy-density aqueous batteries with hydrogen bond-anchored electrolytes. *Matter* 5:162–179
18. Wang X, Xu C, Jaroniec M, Zheng Y, Qiao SZ (2019) Anomalous hydrogen evolution behavior in high-pH environment induced by locally generated hydronium ions. *Nat Commun* 10:4876
19. Wang H, Yang C, Chen F, Zheng G, Han Q (2022) A Crystalline partially fluorinated triazine covalent organic framework for efficient photosynthesis of hydrogen peroxide. *Angew Chem Int Ed* 61:e202202328
20. Yang C, Wan S, Zhu B, Yu J, Cao S (2022) Calcination-regulated microstructures of donor-acceptor polymers towards enhanced and stable photocatalytic H₂O₂ production in pure water. *Angew Chem Int Ed* 61:e202208438
21. Xu X et al (2023) Anthraquinone-based conjugated organic polymers containing dual oxidation centers for photocatalytic H₂O₂ production from H₂O and O₂ under visible-light irradiation. *ACS Appl Poly Mater* 9:7571–7580
22. Xu X et al (2022) Conjugated organic polymers with anthraquinone redox centers for efficient photocatalytic hydrogen peroxide production from water and oxygen under visible light irradiation without any additives. *ACS Catal* 12:12954–12963
23. Ye YX et al (2021) A solar-to-chemical conversion efficiency up to 0.26% achieved in ambient conditions. *Proc. Natl. Acad. Sci. U S A* 118, e2115666118
24. Zhang X et al (2023) Keto-enamine-based covalent organic framework with controllable anthraquinone moieties for superior H₂O₂ photosynthesis from O₂ and water. *Chem Eng J* 466:143085

25. Kandambeth S et al (2012) Construction of crystalline 2D covalent organic frameworks with remarkable chemical (acid/base) stability via a combined reversible and irreversible route. *J Am Chem Soc* 134:19524–19527
26. Wu S et al (2023) The Keto-switched photocatalysis of reconstructed covalent organic frameworks for efficient hydrogen evolution. *Angew Chem Int Ed* 135:e202309026
27. Li Q et al (2020) Visible-light-responsive anthraquinone functionalized covalent organic frameworks for metal-free selective oxidation of sulfides: effects of morphology and structure. *ACS Catal* 10:6664–6675
28. DeBlase CR, Silberstein KE, Truong TT, Abruna HD, Dichtel WR (2013). beta-Ketoenamine-linked covalent organic frameworks capable of pseudocapacitive energy storage. *J Am Chem Soc* 135:16821–16824
29. Khayum MA et al (2016) Chemically delaminated free-standing ultrathin covalent organic nanosheets. *Angew Chem Int Ed* 55:15604–15608
30. Dubois M et al (2011) Solid state NMR study of nanodiamond surface chemistry. *Solid State Nucl Magn Reson* 40:144–154
31. Wu Z et al (2021) Covalent-organic frameworks with keto-enol tautomerism for efficient photocatalytic oxidative coupling of amines to imines under visible light. *Sci Chi Chem* 64:169–2179
32. Chen S et al (2021) Chemical identification of catalytically active sites on oxygen-doped carbon nanosheet to decipher the high activity for electro-synthesis hydrogen peroxide. *Angew Chem Int Ed* 133:16743–16750
33. Zhang L et al (2020) A facile solution-phase synthetic approach for constructing phenol-based porous organic cages and covalent organic frameworks. *Green Chem* 22:2498–2504
34. Zhang M et al (2021) Construction of flexible amine-linked covalent organic frameworks by catalysis and reduction of formic acid via the eschweiler-clarke reaction. *Angew Chem Int Ed* 60:12396–12405
35. Chiang Y, Kresge AJ, Santaballa JA, Wirz J (1988) Ketonization of acetophenone enol in aqueous buffer solutions. Rate-equilibrium relations and mechanism of the uncatalyzed reaction. *J Am Chem Soc* 110:5506–5510
36. Li L, Xu L, Hu Z, Yu JC (2021) Enhanced mass transfer of oxygen through a gas-liquid-solid interface for photocatalytic hydrogen peroxide production. *Adv Funct Mater* 22:2106120
37. Chu C et al (2022) Photocatalytic H₂O₂ production driven by cyclodextrin-pyrimidine polymer in a wide pH range without electron donor or oxygen aeration. *Appl Catal B: Environ* 314:121485
38. Yu FY, Zhou YJ, Tan HQ, Li YG, Kang ZH (2023) Versatile photoelectrocatalysis strategy raising up the green production of hydrogen peroxide. *Adv Energy Mater* 13:202300119
39. Mitsui T, Rose MK, Fomin E, Ogletree DF, Salmeron M (2002) Water diffusion and clustering on Pd(111). *Science* 297:1850–1852
40. Peng J et al (2018) The effect of hydration number on the interfacial transport of sodium ions. *Nature* 557:701–705

41. Nilsson A, Pettersson LG (2015) The structural origin of anomalous properties of liquid water. *Nat Commun* 6:8998
42. Shen R et al (2023) Coupling oxygen vacancy and hetero-phase junction for boosting catalytic activity of Pd toward hydrogen generation. *Appl Catal B: Environ* 328:122484
43. Wang YH et al (2021) In situ Raman spectroscopy reveals the structure and dissociation of interfacial water. *Nature* 600:81–85
44. Chen S et al (2022) Aqueous rechargeable zinc air batteries operated at -110°C. *Chem* 9:497–510
45. Zeng H et al (2020) pH-independent production of hydroxyl radical from atomic H*-Mediated electrocatalytic H₂O₂ reduction: a green fenton process without byproducts. *Environ Sci Technol* 54:14725–14731
46. Liu R et al (2018) Defect sites in ultrathin Pd nanowires facilitate the highly efficient electrochemical hydrodechlorination of pollutants by H*_{ads}. *Environ Sci Technol* 52:9992–10002
47. Strmcnik D et al (2009) The role of non-covalent interactions in electrocatalytic fuel-cell reactions on platinum. *Nat Chem* 1:466–472
48. Wei Y et al (2021) Quantification of photocatalytically-generated hydrogen peroxide in the presence of organic electron donors: Interference and reliability considerations. *Chemosphere* 279:130556
49. Gu S et al (2019) Tunable redox chemistry and stability of radical intermediates in 2D covalent organic frameworks for high performance sodium ion batteries. *J Am Chem Soc* 141:9623–9628

Figures

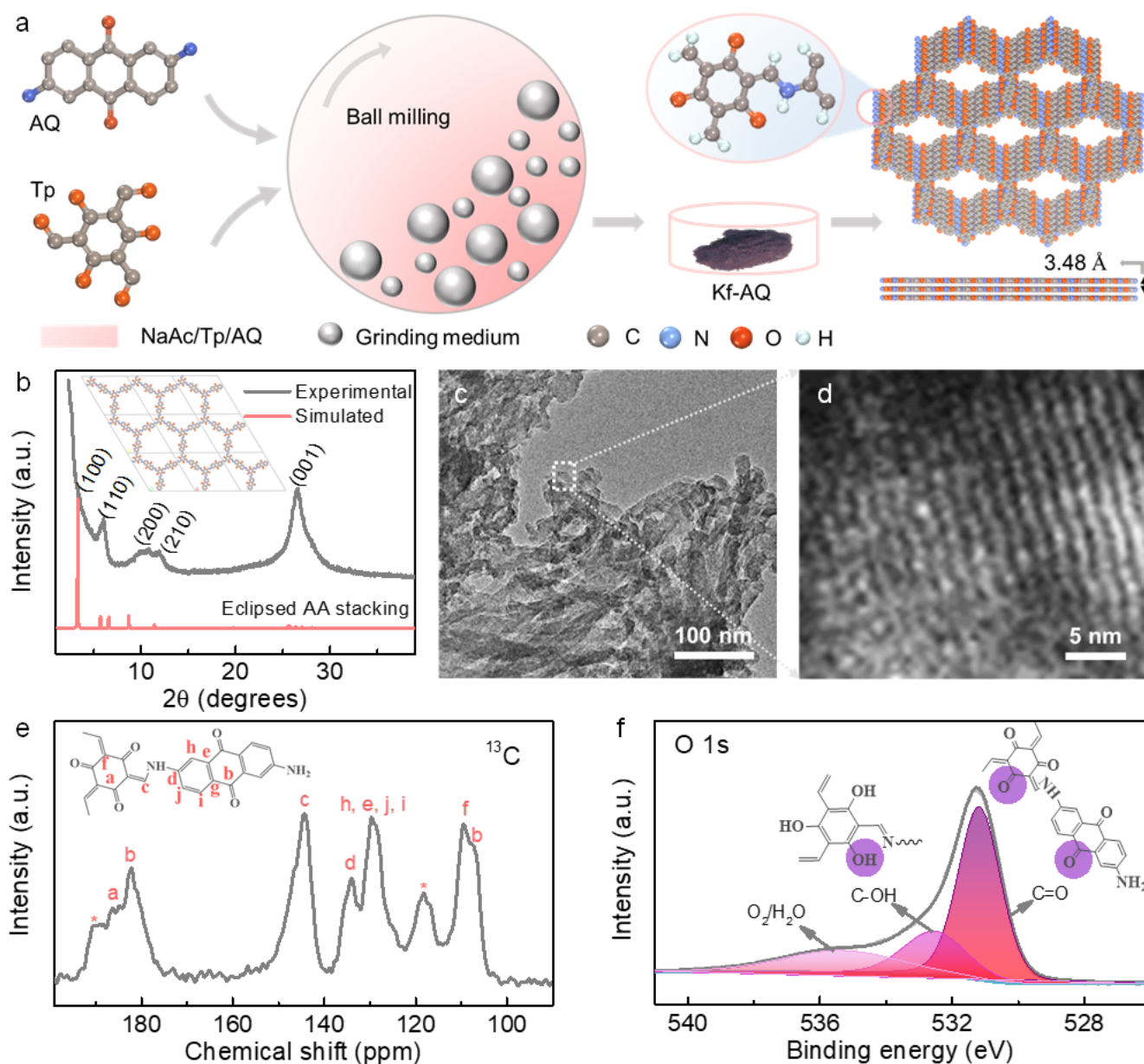


Figure 1

Synthesis process and structural characterization. (a) Schematic of Kf-AQ condensation; (b) PXRD patterns of Kf-AQ, experimentally observed (dark) and simulated using eclipsed AA-stacking (red); the inset is the crystal structures of the eclipsed AA stacking model, the simulated cell parameters of a, b and c are 30.59, 30.59 and 3.51 Å, respectively; (d, f) TEM images of Kf-AQ; (e) ¹³C CP-MAS solid state NMR spectra of Kf-AQ; the inset is the molecular moiety of Kf-AQ; (f) high-resolution O1s XPS spectra for Kf-AQ.

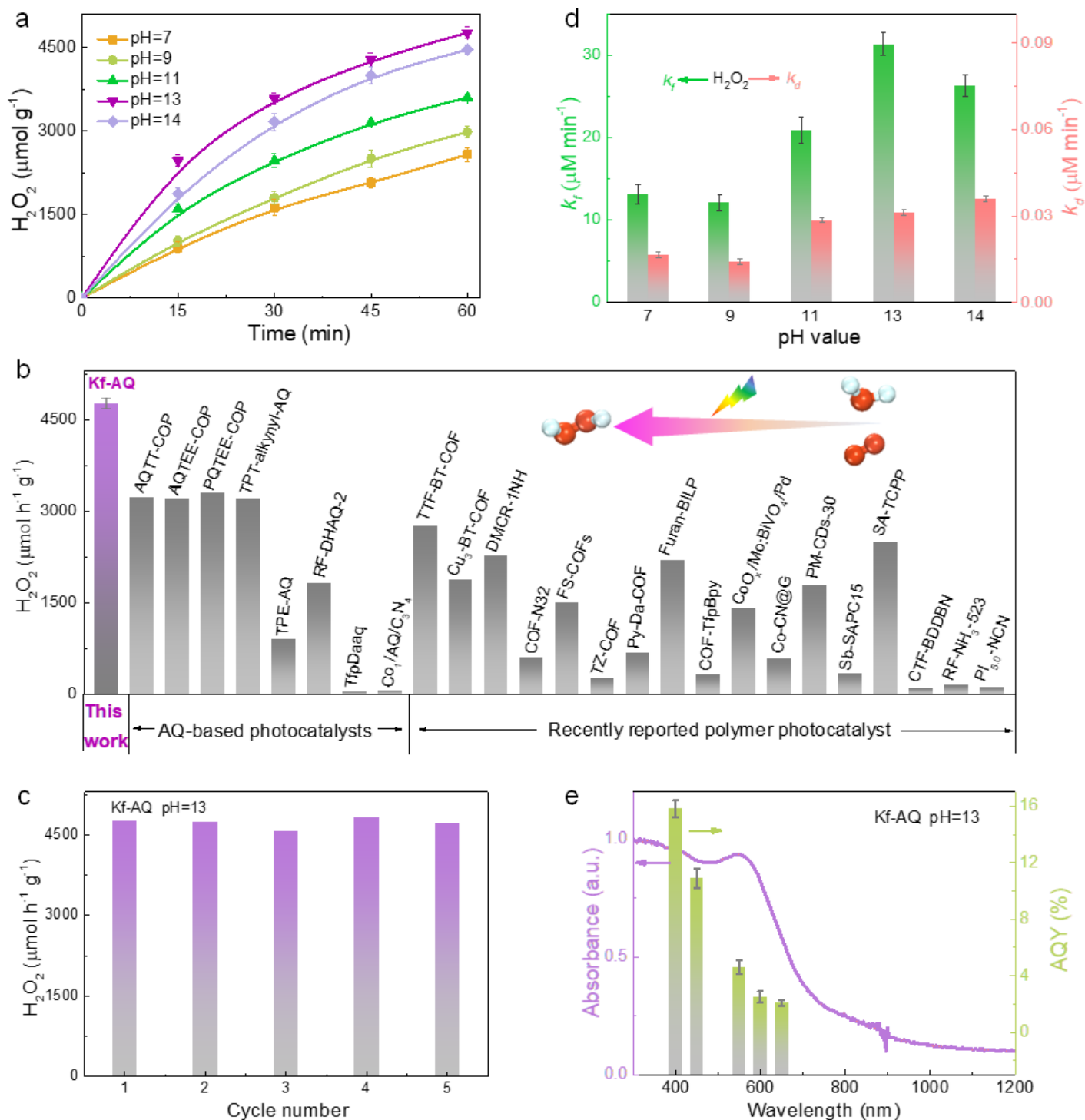


Figure 2

H₂O₂ photosynthesis. (a) Photocatalytic H₂O₂ production at different pH conditions; (b) a comparison of photocatalytic H₂O₂ production rates for photocatalysts in the absence of sacrificial reagents; (c) the recycling tests of Kf-AQ at pH=13; (d) the rate constants of H₂O₂ formation (k_f) and decomposition (k_d); (e) wavelength-dependent AQY of photocatalytic H₂O₂ production on Kf-AQ at pH=13.

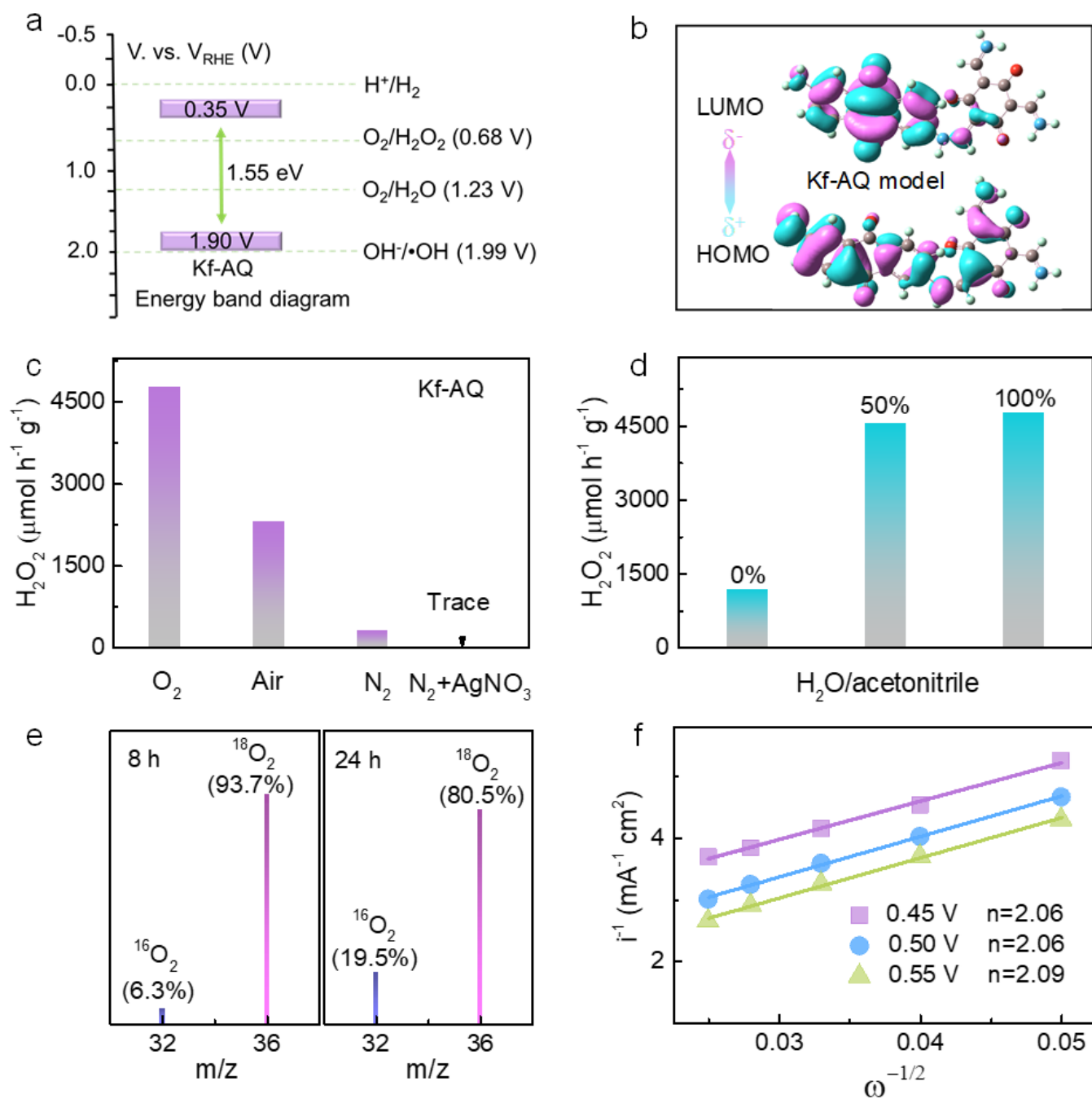


Figure 3

Mechanism investigation. (a) Band edge potentials of Kf-AQ; (b) calculated HOMO and LUMO for Kf-AQ dimer; (c, d) a comparison on H_2O_2 production rates over Kf-AQ in different atmospheres and solutions; (e) mass charts for O_2 evolved by decomposition of H_2O_2 produced at pH 13 by isotopic experiments; (f) the Koutecky-Levich plots of Kf-AQ obtained by RDE measurements.

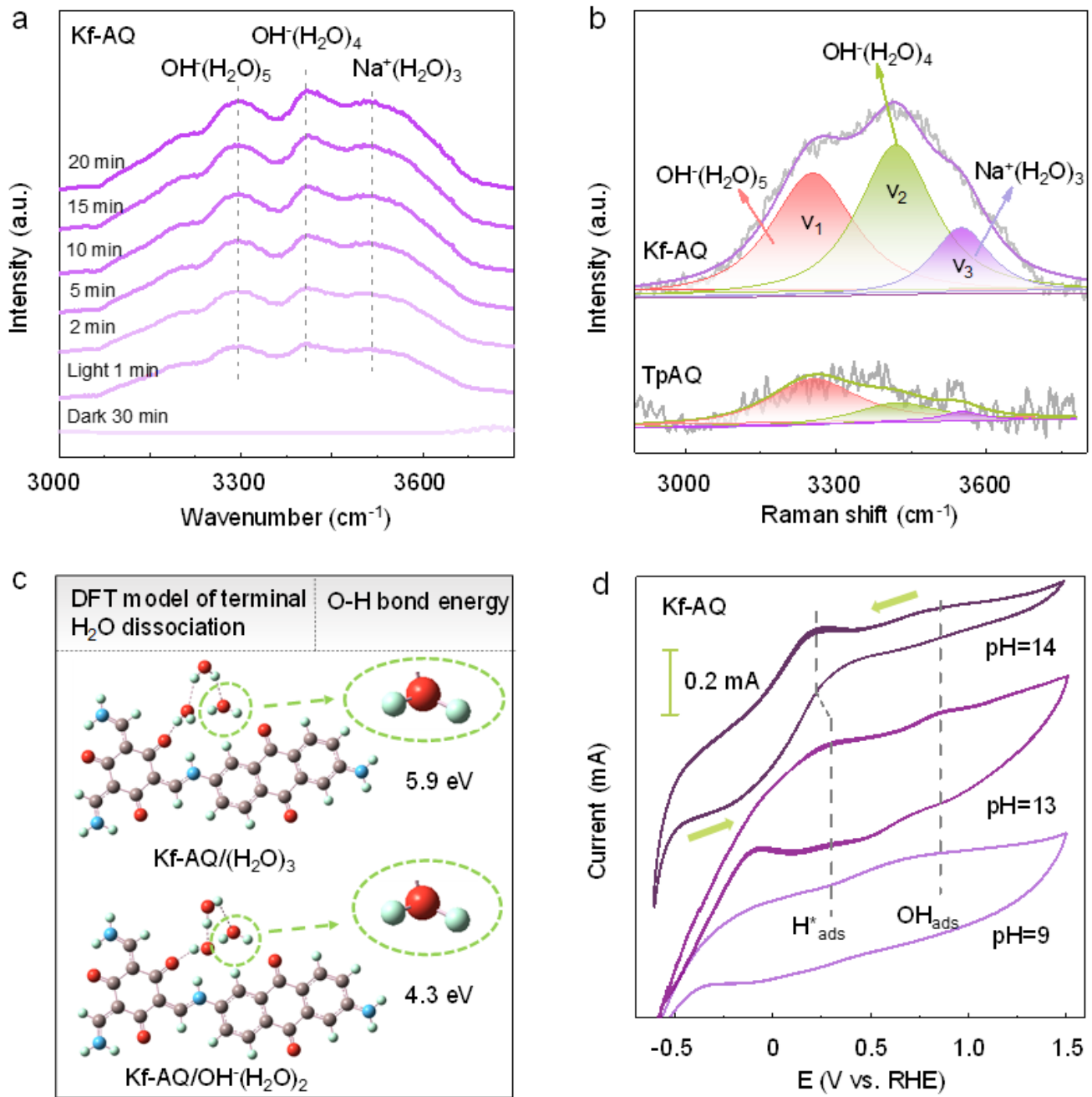


Figure 4

Mechanism investigation. (a) In-situ FTIR spectra of Kf-AQ suspension for H_2O_2 photosynthesis; (b) Raman spectra of Kf-AQ and TpAQ suspensions under visible light irradiation; (c) the H-O bond energy of the adsorbed terminal H_2O over the Kf-AQ via DFT calculation; (d) cyclic voltammogram (CV) curves of Kf-AQ in different pH electrolytes.

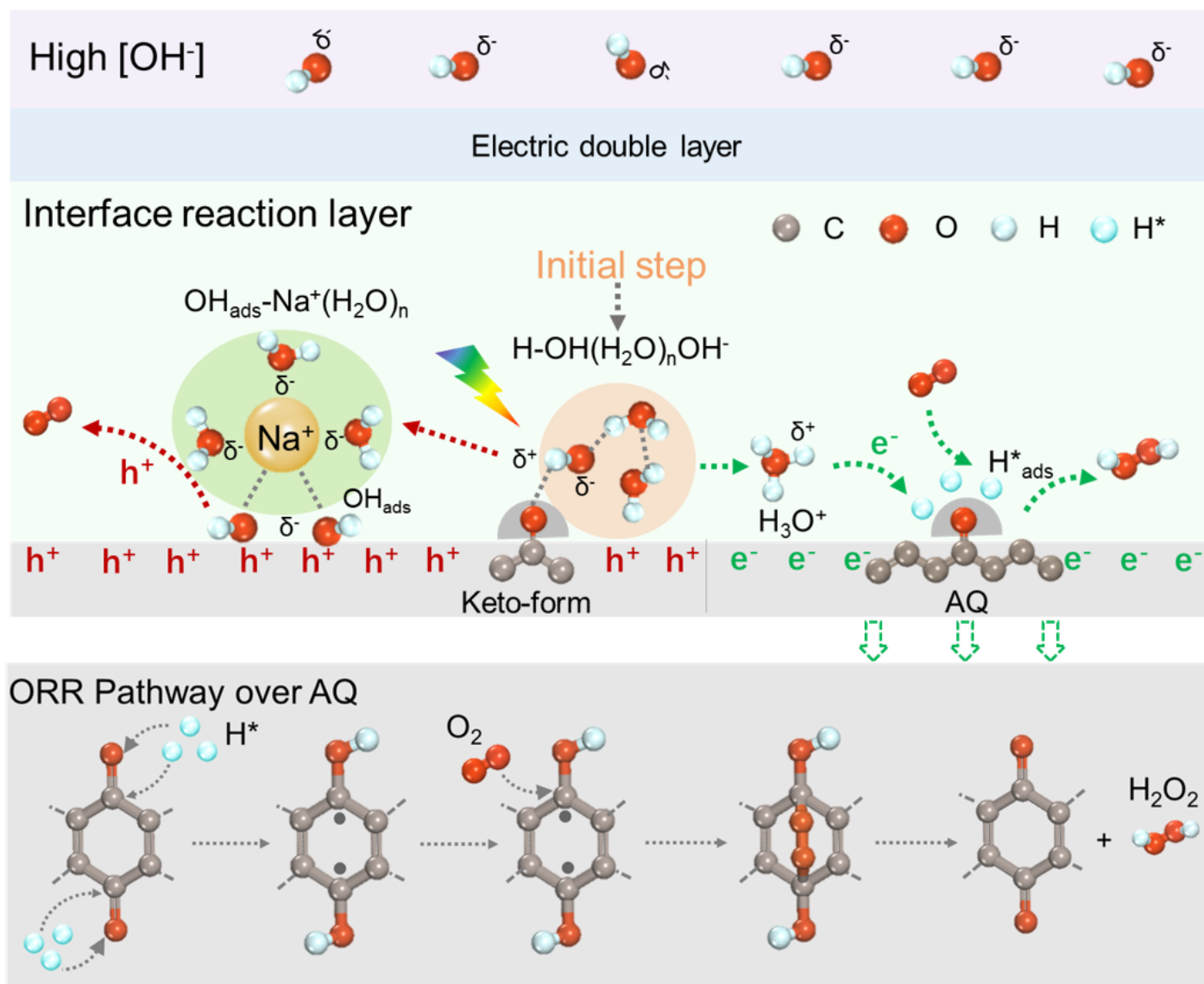


Figure 5

Mechanism of H₂O₂ photosynthesis. The photocatalytic pathway for H₂O₂ production over Kf-AQ in alkaline conditions.

Supplementary Files

This is a list of supplementary files associated with this preprint. Click to download.

- [Supplementaryinformation.docx](#)